Journal of Quantitative Spectroscopy & Radiative Transfer 319 (2024) 108957

Contents lists available at ScienceDirect

Journal of Quantitative Spectroscopy and Radiative Transfer

journal homepage: www.elsevier.com/locate/jqsrt

Radiative transfer in luminescent solar concentrators

Sha Li, Sophia Haussener *

Laboratory of Renewable Energy Science and Engineering, EPFL, Station 9, Lausanne 1015, Switzerland

ARTICLE INFO

Keywords:
Luminescent solar concentrator
Modified radiative transfer equation
Monte Carlo ray tracing
Lumogen F Red 305 dye
performance optimization

ABSTRACT

A luminescent solar concentrator (LSC) offers a viable solution to spectrally convert and concentrate both direct and diffuse sunlight without the need for tracking. Its potential for commercialization is currently limited by the optical performance. A detailed understanding of the effects of both waveguide and luminophore properties is crucial for designing efficient LSCs. Herein, a self-consistent modelling framework of radiative transfer in LSCs is presented to analyze these effects by incorporating all properties at multiple length scales. A modified radiative transfer equation (RTE) is derived capturing the requirement that both photon absorption and photoluminescence quantum yield (PLQY) should occur simultaneously to trigger the PL emission. The Monte Carlo method is used to solve this modified RTE along with its boundary conditions. This framework is further employed to investigate the performance of LSCs doped with Lumogen F Red 305 (LFR305) dye. For the realistic scenarios, the transmission loss forms the main loss mechanism and accounts for 72.6–92.1% depending on the specific dimensions and LFR305 doping. An external photon efficiency of 13.0% is predicted for an LSC of $20 \times 20 \times 0.5$ cm^3 with a dye concentration of 5×10^{-4} mol/L. As to the hypothetical scenarios, the waveguide refractive index affects both the top reflection and the escape cone losses, while in contrast, the PLQY and the Stokes shift mainly affect the QY loss. Future efforts on LSC optimization should be directed towards reducing the transmission loss.

1. Introduction

A luminescent solar concentrator (LSC) is a promising photonic technology with potential applications in, for example, building-integrated photovoltaic structures, horticulture, photochemical reactors, or smart windows [1]. An LSC is typically composed of a waveguide doped or coated with well-quantified concentrations of one or more luminophore species, including organic dyes, inorganic phosphors, and quantum dots. Such a design allows the sunlight incident on the top surface to be absorbed by the luminophore(s), and then emitted at a different wavelength in the form of photoluminescence (PL), which will be transported to the edges via total internal reflection (TIR), thus achieving spectral conversion and light concentration (see Fig. 1). Compared with the conventional solar concentrating technologies, LSC offers the advantages of being able to utilize both direct and diffuse sunlight without tracking, and the flexibility to tune its PL emission spectrum by using different luminophores [1]. However, the LSC is not yet commercialized primarily due to its modest performance (record external photon efficiency so far is 11.7% [2]).

Computational models have been developed to predict the performance of a variety of LSC concepts. They fall into two categories: (*i*) thermodynamic modelling [3–6], and (*ii*) Monte Carlo (MC) ray tracing simulations [7–9]. The thermodynamic approach [3,4] is essentially a 3D flux model claimed to not require the PL emission spectrum as an input, and its application is limited to those LSCs containing a single luminophore species [10]. However, this 3D flux model [3,4] is obtained by performing integration over a range of solid angles for the radiative transfer equation (RTE) following the Schwarzschild–Milne Method, which is valid only for 1D, plane-parallel, and isotropic scattering media [11]. In addition, the RTE and the total radiative energy balance equation in Refs. [3,5,6] remain inconsistent, for the former cannot directly lead to the latter without providing the quantum yield (QY). It is thus desirable to develop a self-consistent, 3D modelling framework with respect to the spectral intensity as it travels within the LSC. As to the MC method, a number of ray tracing codes have been developed for specific LSCs with different geometries (planar, cylindrical, wedge-shaped, etc.), configurations (doped, thin-film, single layer, multi-layer, etc.), and

Abbreviations: AM1.5D, air mass 1.5 direct; LFR305, Lumogen F Red 305; LSC, luminescent solar concentrator; MC, Monte Carlo; PL, photoluminescence; PMMA, poly(methyl methacrylate); QY, quantum yield; RHS, right-hand side; RTE, radiative transfer equation; TIR, total internal reflection.

* Corresponding author.
E-mail address: sophia.haussener@epfl.ch (S. Haussener).

https://doi.org/10.1016/j.jqsrt.2024.108957
Received 12 December 2023; Received in revised form 23 February 2024; Accepted 29 February 2024
Available online 5 March 2024

Nomenclature

A_{top},$A_{edge,i}$	area of the top surface and the edge surface i of an LSC (cm^2)
c	speed of light ($m\ s^{-1}$)
C	concentration factor (–)
c_p	molar concentration of luminophore particles (mol/L)
$C_{abs,p}$,$C_{sca,p}$	absorption and scattering cross section of a luminophore particle (m^2)
f^{-1}	inverse function
G	geometric gain (–)
G_λ	spectral incident radiation function ($W\ m^{-2}\ nm^{-1}$)
h	Planck constant ($6.626 \times 10^{-34} J \cdot s$)
H_{LSC}	thickness of an LSC sample (mm)
I_λ	spectral light intensity ($W\ m^{-2}\ nm^{-1}\ sr^{-1}$)
$k_{\lambda,wg}$	absorptive index of the waveguide (–)
l_s	the distance a ray travels to the nearest boundary of a LSC (m)
l_{ext}	extinction distance (m)
L_{LSC}	length of an LSC (cm)
n_{wg}, $n_{wg,hypo}$	refractive index of a waveguide and of a hypothetical waveguide (–)
N_p	number density of luminophore particles (m^{-3})
$\dot{N}_\lambda$	spectral photon rate ($s^{-1}nm^{-1}$)
$P_{PL\lambda,p}$	photoluminescence wavelength function (–)
$\mathbf{q}_{\lambda,rad}$, $\mathbf{q}_{rad}$	spectral and total radiative heat flux ($W\ m^{-2}$)
$R_{\lambda,wg}$, R	spectral reflectivity of a waveguide sample, pseudorandom number (–)
$T_{\lambda,wg}$	spectral transmissivity of a waveguide sample (–)
W_{LSC}	width of an LSC (cm)

Greek symbols

$\alpha_{\lambda,edge}$	spectral absorptivity of the edge surfaces (–)
β_λ	spectral extinction coefficient (cm^{-1})
$\varepsilon_{\lambda,p}$	spectral molar absorption coefficient of luminophore particles ($L\ mol^{-1}\ cm^{-1}$)
δ	Dirac delta function (–)
$\Delta\lambda_S$	Stokes shift (nm)
η_{int},η_{ext}	internal and external photon (or quantum) efficiency (–)
θ_{in},θ'_{in}	dummy angles of incidence (°)
κ_λ, $\bar{\kappa}_\lambda$	spectral absorption coefficient, mean absorption coefficient (cm^{-1})
λ, $\bar{\lambda}_{PL}$	wavelength of light, mean photoluminescence spectrum (nm)
ν	frequency of light (s^{-1})
ρ_λ	spectral bi-directional reflectivity (–)
$\sigma_{s,\lambda}$	spectral scattering coefficient (cm^{-1})
ϕ_{PL}	photoluminescence quantum yield (–)
φ	azimuthal angle (°)
$\psi_{\lambda,source}$	spectral photon flux density of the light source ($s^{-1}\ m^{-2}\ nm^{-1}$)
$\Phi_{PL\lambda,p}$, $\Phi_{s\lambda,p}$	photoluminescence and scattering phase function (–)
ω_λ	single scattering albedo (–)
Ω, Ω', Ω''	solid angles (sr)

Subscripts

0	vacuum condition
abs	absorption
btm	Bottom surface of an LSC
ext	extinguished
hypo	hypothetical
in	incidence direction
max	maximum value
min	minimum value
p	luminophore particles
r, refract	refraction direction
rad	radiative
S	Stokes shift
s, sca	scattering
w	wall
wg	waveguide

luminophore properties (scattering, non-scattering) [7–9]. Nonetheless, most of the MC work is focused on detailing the history of each photon during the ray tracing process, and very few efforts have been made to describe the governing equation and boundary conditions in order to offer a clear picture of this problem. The lack of a well-stated governing equation in the MC method perhaps helps explain the fact that the thermodynamic model and the MC method have long been viewed as two different approaches [8,10]. On the other hand, Kennedy et al. [10] showed that the predicted LSC performance based on these two methods is in agreement, which motivates us to hypothesize that the thermodynamic model and the MC method are equivalent. This is for example the case in the high-temperature thermal community where the MC method is widely employed to solve the conventional RTE for participating media in the absence of PL emission [11–13].

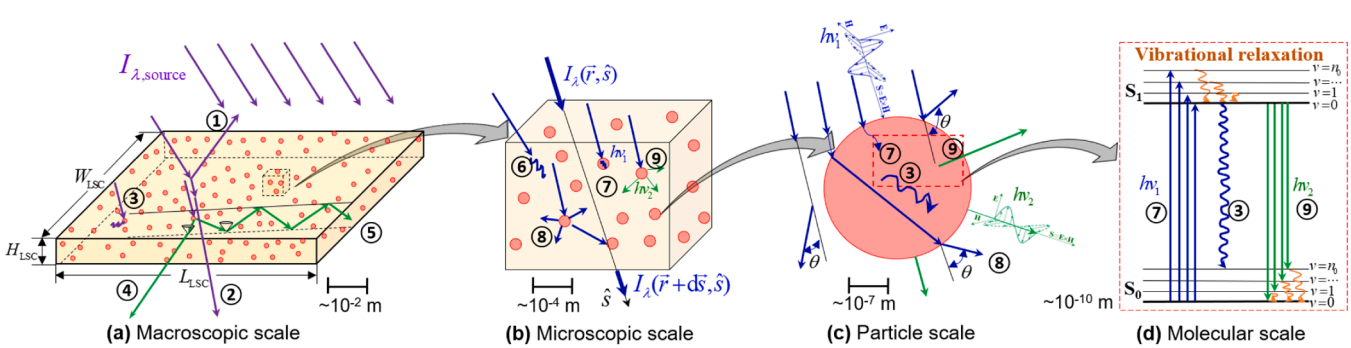

Fig. 1. Schematic of (a) the LSC model system irradiated by a light source at the macroscopic scale, (b) an infinitesimal volume at the microscopic scale used to derive the modified RTE, and relevant light–matter interactions at (c) the luminophore particle scale, and (d) the luminophore molecular scale using Jablonski diagram. The circled numbers represent: ① light reflection at the top surface, ② light transmission through the bottom surface, ③ QY loss, ④ escape cone loss, ⑤ light collection at edges due to TIR by the waveguide, ⑥ light absorption by the waveguide, ⑦ light absorption and ⑧ light scattering by the luminophore particles, and ⑨ PL emission from the luminophore particles. The spherical luminophore particles can be of any arbitrary shape and can be aligned either randomly or at a certain tilt angle.

Herein, we first present a generic modelling framework of radiative transfer in LSCs by making an energy balance for the spectral intensity, with an emphasis on analyzing the PL emission from the luminophore. A modified RTE is derived, based on which the total radiative energy balance equation is obtained via integration over all solid angles and the full spectrum, thus demonstrating model self-consistency without additional input. To solve this modified RTE along with its associated boundary conditions, the MC method is employed, which confirms the hypothesis that the thermodynamic model and the MC approach are equivalent. To demonstrate its application, this methodology was applied to a specific LSC composed of poly(methyl methacrylate) (PMMA) as the waveguide doped with a commercial dye Lumogen F Red 305 (LFR305). Its performance under both realistic and hypothetical scenarios are explored in order to offer insights on performance optimization.

2. Methodology

The model system is a 3D planar LSC doped with well-defined concentration of luminophores (e.g. with dyes, quantum dots, or phosphors) as shown in Fig. 1, which also illustrates the key light–matter interactions at multiple length scales. Note that the luminophore particles can be aligned either randomly [14] or at a certain tilt angle [15]. To model the radiative transport within the LSC, unlike the conventional RTE derived for a participating medium in the absence of PL emission, a modified RTE will be developed to account for this effect based on the radiative energy balance.

The following assumptions are made: (*i*) the LSC is treated as a homogeneous medium with luminophores being uniformly distributed within the waveguide matrix; (*ii*) the LSC medium is stationary, non-polarizing, and at local thermodynamic equilibrium [11], justifying the quasi-steady radiative transfer treatment in the LSC; (*iii*) light is only scattered by the luminophore particles in an elastic manner, and light scattering by the waveguide matrix is hence not considered; (*iv*) the characteristic length of the infinitesimal volume (Fig. 1b) is assumed much larger than the wavelength of both the incident light and the PL emission such that the laws of geometric optics are valid; (*v*) the LSC medium has a constant refractive index, so the light travels through it along straight lines; (*vi*) the top, bottom and all edge surfaces of the LSC are assumed optically smooth; (*vii*) the absorptive index of most waveguides (glass, PMMA, di-ureasil) is usually far lower (at least two orders of magnitude) than their refractive index in the AM 1.5 standard spectrum [16,17], such that light reflection and refraction at the waveguide–air interface can be modelled via Snell's law and Fresnel's relation; (*viii*) all edge surfaces are treated as perfect absorber in an ideal application context where either a solar cell (for electricity generation) or a micro reactor (for chemical production) is attached to each edge using index-matching glue; (*ix*) the LSC is assumed a cold medium, so blackbody intensity at the medium temperature is neglected; and (*x*) the luminophore particles are of uniform size and shape, so particle size effects are not considered.

2.1. Modified radiative transfer equation

Attenuation by absorption and out-scattering. Similar to the phenomena involved in deriving the conventional RTE, the spectral light intensity in the LSC can be attenuated due to light absorption by the waveguide, as well as light absorption and out-scattering (assumption (*iii*)) by the luminophore particles:

$$\left.\frac{\mathrm{d}I_\lambda(\vec{r},\hat{s})}{|\mathrm{d}\vec{s}|}\right|_{\text{attenuated}} = -\left(\kappa_{\lambda,\mathrm{wg}} + \kappa_{\lambda,\mathrm{p}}(\hat{s}) + \sigma_{\mathrm{s}\lambda,\mathrm{p}}\right) I_\lambda(\vec{r},\hat{s}) \tag{1}$$

where $\kappa_{\lambda,\mathrm{wg}}$, $\kappa_{\lambda,\mathrm{p}}$, and $\sigma_{\mathrm{s}\lambda,\mathrm{p}}$ are the spectral absorption coefficient of the waveguide, the spectral absorption and scattering coefficients of the luminophore particles, respectively. Note that the luminophore absorption coefficient is usually anisotropic for materials like organic dyes [14,18] and non-spherical quantum dots [19]. The sum of all three coefficients are termed as the spectral extinction coefficient β_λ. The single scattering albedo $\omega_\lambda$is defined as:

$$\omega_\lambda = \frac{\sigma_{\mathrm{s}\lambda,\mathrm{p}}}{\beta_\lambda}, \text{ with } \beta_\lambda = \kappa_{\mathrm{s}\lambda,\mathrm{wg}} + \kappa_{\mathrm{s}\lambda,\mathrm{p}} + \sigma_{\mathrm{s}\lambda,\mathrm{p}} \tag{2}$$

which will facilitate the description of the MC method in Section 2.4. The determination of these coefficients will be discussed in Section 2.2.

Augmentation by in-scattering and PL emission. Different from the conventional RTE applied to cold media (assumption (*ix*)) where beam augmentation purely comes from light in-scattering, a new contribution in the LSC is the PL emission from the luminophore particles:

$$\begin{aligned}\left.\frac{\mathrm{d}I_\lambda(\vec{r},\hat{s})}{|\mathrm{d}\vec{s}|}\right|_{\text{augmented}} &= \frac{\sigma_{\mathrm{s}\lambda,\mathrm{p}}}{4\pi}\int_{4\pi} I_\lambda(\vec{r},\hat{s}')\Phi_{\mathrm{s}\lambda,\mathrm{p}}(\hat{s}',\hat{s})\mathrm{d}\Omega' \\ &+\frac{1}{4\pi}\int_{4\pi}\int_{\lambda_{\mathrm{abs,min}}}^{\lambda_{\mathrm{abs,max}}} \kappa_{\lambda,\mathrm{p}}(\lambda_{\mathrm{abs}},\hat{s}'')I_\lambda(\lambda_{\mathrm{abs}},\vec{r},\hat{s}'')\cdot\phi_{\mathrm{PL}}(\lambda_{\mathrm{abs}})\frac{\lambda_{\mathrm{abs}}}{\lambda}\mathrm{d}\lambda_{\mathrm{abs}}\cdot P_{\mathrm{PL}\lambda,\mathrm{p}}(\lambda)\cdot\Phi_{\mathrm{PL}\lambda,\mathrm{p}}(\hat{s})\mathrm{d}\Omega''\end{aligned} \tag{3}$$

where $\Phi_{\mathrm{s}\lambda,\mathrm{p}}$, ϕ_{PL}, $P_{\mathrm{PL}\lambda,\mathrm{p}}$and $\Phi_{\mathrm{PL}\lambda,\mathrm{p}}$are the scattering phase function, the photoluminescence quantum yield (PLQY), the PL wavelength function, and the PL phase function of the luminophore particles, respectively. The dummy symbols of Ω' and Ω''denote the incoming solid angles. The first term on the right-hand side (RHS) of Eq. (3) is the rate of light in-scattering by the luminophore particles from all other incoming directions $\hat{s}'$ into the propagation direction $\hat{s}$; while the second term on the RHS represents the rate of PL emission after absorbing all incoming photons from all directions $\hat{s}''$ within the range of absorption spectrum λ_{abs}. The PLQY in Eq. (3) is a quantum-based property defined as the ratio of the PL emitted photons to the absorbed ones per unit time, $\phi_{\mathrm{PL}} = \dot{N}_\lambda/\dot{N}_{\lambda,\mathrm{abs}}$, and can be dependent [20] or independent [21] of the excitation wavelength, depending on the specific luminophore material. Due to the non-radiative decay effect such as luminescence quenching, not every photon that is absorbed by the luminophore will be emitted via PL, leading to non-unity PLQY. The combined term $\phi_{\mathrm{PL}}\cdot\lambda_{\mathrm{abs}}/\lambda$ in Eq. (3) serves to account for the energy difference between the absorbed intensity and the PL emission intensity due to Stokes shift effect:

$$\frac{I_\lambda}{I_{\lambda,\mathrm{abs}}} = \frac{\dot{N}_\lambda\cdot h\nu}{\dot{N}_{\lambda,\mathrm{abs}}\cdot h\nu_{\mathrm{abs}}} = \frac{\dot{N}_\lambda}{\dot{N}_{\lambda,\mathrm{abs}}}\frac{\lambda_{\mathrm{abs}}}{\lambda} = \frac{\phi_{\mathrm{PL}}\lambda_{\mathrm{abs}}}{\lambda} \tag{4}$$

The PL wavelength function $P_{\mathrm{PL}\lambda,\mathrm{p}}(\lambda)$ appearing in Eq. (3) describes the probability that a photon will be emitted at wavelength λ via PL. It is assumed independent from the absorbed wavelength, because PL emission usually occurs from the lowest excited electronic state regardless of the vibrational level of the excited electron state after photon absorption, a phenomenon known as Kasha's rule [22]. Consequently, the following relation will be automatically satisfied:

$$\int_{\lambda_{\mathrm{PL,min}}}^{\lambda_{\mathrm{PL,max}}} P_{\mathrm{PL}\lambda,\mathrm{p}}(\lambda)\,\mathrm{d}\lambda = 1 \tag{5}$$

The PL wavelength function $P_{\mathrm{PL}\lambda,\mathrm{p}}$is a unique characteristic of the specific luminophore material, and can be obtained from its normalized emission spectrum intensity.

Finally, the PL phase function $\Phi_{\mathrm{PL}\lambda,\mathrm{p}}$ in Eq. (3) describes the probability that a photon will be emitted into direction $\hat{s}$ via PL, and follows a similar definition to the scattering phase function:

$$\frac{1}{4\pi}\int_{4\pi} \Phi_{\mathrm{PL}\lambda,\mathrm{p}}(\hat{s})\mathrm{d}\Omega = 1 \tag{6}$$

where Ω represents the outgoing solid angle. Luminophore materials such as most organic dyes [14,23] and non-spherical quantum dots [19] usually emit in an anisotropic manner. , If the PL emission from a luminophore is isotropic, we have $\Phi_{\mathrm{PL}\lambda,\mathrm{p}}(\hat{s}) = 1$. The determination of $\Phi_{\mathrm{s}\lambda,\mathrm{p}}$, ϕ_{PL}, $P_{\mathrm{PL}\lambda,\mathrm{p}}$ and $\Phi_{\mathrm{PL}\lambda,\mathrm{p}}(\hat{s})$ will be described in Section 2.2.

Radiative energy balance. The change in spectral intensity in the LSC is found by summing up all contributions, Eqs. (1) and (3), leading to the following modified RTE:

$$\begin{aligned}\hat{s}\cdot\nabla I_\lambda(\vec{r},\hat{s}) \;=\; & -\left(\kappa_{\lambda,\mathrm{wg}} + \kappa_{\lambda,\mathrm{p}}(\hat{s}) + \sigma_{\mathrm{s}\lambda,\mathrm{p}}\right) I_\lambda(\vec{r},\hat{s}) + \frac{\sigma_{\mathrm{s}\lambda,\mathrm{p}}}{4\pi}\int_{4\pi} I_\lambda(\vec{r},\hat{s}')\Phi_{\mathrm{s}\lambda,\mathrm{p}}(\hat{s}',\hat{s})\mathrm{d}\Omega' \\ & + \frac{1}{4\pi}\frac{1}{\lambda}P_{\mathrm{PL}\lambda,\mathrm{p}}(\lambda)\cdot\Phi_{\mathrm{PL}\lambda,\mathrm{p}}(\hat{s})\int_{\lambda_{\mathrm{abs,min}}}^{\lambda_{\mathrm{abs,max}}} \phi_{\mathrm{PL}}(\lambda_{\mathrm{abs}})\,\lambda_{\mathrm{abs}}\,\bar{\kappa}_{\lambda,\mathrm{p}}(\lambda_{\mathrm{abs}})G_\lambda(\lambda_{\mathrm{abs}},\vec{r})\cdot\mathrm{d}\lambda_{\mathrm{abs}}\end{aligned} \tag{7}$$

where we have introduced the spectral incident radiation function$G_\lambda = \int_{4\pi} I_\lambda(\vec{r},\hat{s}'')\mathrm{d}\Omega''$, and the mean spectral absorption coefficient $\bar{\kappa}_{\lambda,\mathrm{p}}$ defined as:

$$\bar{\kappa}_{\lambda,\mathrm{p}} = \frac{\int_{4\pi}\kappa_{\lambda,\mathrm{p}} I_\lambda(\vec{r},\hat{s}'')\mathrm{d}\Omega''}{\int_{4\pi} I_\lambda(\vec{r},\hat{s}'')\mathrm{d}\Omega''} \tag{8}$$

and exchanged the order of integration over wavelength and solid angle given their independence. Compared with the conventional RTE applicable for participating media in the absence of PL emission [11], the modified RTE, Eq. (7), incorporates a new term at the end of its RHS to account for the PL emission effect, which introduces additional challenge in solving it. In addition, unlike the RTE of LSC in Ref. [6] that treats photon absorption and PL emission independently without the need for PL emission spectrum, our Eq. (7) requires the inputs of absorption and PL emission spectra as well as PLQY. This fundamentally respects that both photon absorption and PLQY should occur simultaneously in order to trigger the PL emission. Failing to capture this fact in Ref. [6] is the source of model inconsistency between its RTE and the total radiative energy balance equation. A similar modified RTE is also found in literature [24–26] for a different application—phosphor-converted light-emitting diodes.

To get the net radiative energy balance within an infinitesimal volume (Fig. 1b), Eq. (7) can be integrated over all solid angles, and its final version becomes:

$$\begin{aligned}\nabla\cdot\mathbf{q}_{\lambda,\mathrm{rad}} \;=\; & -\left(\kappa_{\lambda,\mathrm{wg}} + \bar{\kappa}_{\lambda,\mathrm{p}}(\lambda)\right)G_\lambda \\ & + \frac{1}{\lambda}P_{\mathrm{PL}\lambda,\mathrm{p}}(\lambda)\int_{\lambda_{\mathrm{abs,min}}}^{\lambda_{\mathrm{abs,max}}} \phi_{\mathrm{PL}}(\lambda_{\mathrm{abs}})\,\lambda_{\mathrm{abs}}\,\bar{\kappa}_{\lambda,\mathrm{p}}(\lambda_{\mathrm{abs}})G_\lambda(\lambda_{\mathrm{abs}},\vec{r})\,\mathrm{d}\lambda_{\mathrm{abs}}\end{aligned} \tag{9}$$

The divergence of the total radiative heat flux can be further acquired by performing integration over the spectrum for Eq. (9):

$$\nabla\cdot\mathbf{q}_{\mathrm{rad}} = -\int_0^\infty \kappa_{\lambda,\mathrm{wg}}G_\lambda\mathrm{d}\lambda - \int_0^\infty\left(1 - \frac{\phi_{\mathrm{PL}}(\lambda)\cdot\lambda}{\bar{\lambda}_{\mathrm{PL}}}\right)\cdot\bar{\kappa}_{\lambda,\mathrm{p}}G_\lambda\mathrm{d}\lambda \tag{10}$$

where we have introduced the mean emission spectrum:

$$\frac{1}{\bar{\lambda}_{\mathrm{PL}}} = \int_{\lambda_{\mathrm{PL,min}}}^{\lambda_{\mathrm{PL,max}}} \frac{1}{\lambda}P_{\mathrm{PL}\lambda,\mathrm{p}}(\lambda)\mathrm{d}\lambda. \tag{11}$$

Eq (10) states that the net radiative energy loss within an infinitesimal volume is equal to the absorbed radiation by the waveguide plus the radiation loss from the luminophore due to the change in wavelength between absorption and PL emission spectra. Different from the self-inconsistent thermodynamic model developed in Refs [3,5,6], our modified RTE (Eq. (7)) and the total radiative energy balance equation (Eq. (10)) here are mutually consistent without additional input.

2.2. Determination of photophysical properties

The photophysical properties appearing in Eq. (7) can be determined using combined theoretical and experimental techniques. The absorption coefficient of the waveguide matrix $\kappa_{\lambda,\mathrm{wg}}$ is a purely material-dependent property, and can be readily determined from the electromagnetic theory [27]:

$$\kappa_{\lambda,\mathrm{wg}} = \frac{4\pi k_{\lambda,\mathrm{wg}}}{\lambda_0} \tag{12}$$

where $k_{\lambda,\mathrm{wg}}$ and λ_0 are the absorptive index of the waveguide and the wavelength of the light in vacuum. Alternatively, one can refer to the UV–Vis spectroscopy technique to measure both the spectral reflectivity $R_{\lambda,\mathrm{wg}}$ and transmissivity $T_{\lambda,\mathrm{wg}}$ of the waveguide based on the following relation:

$$\kappa_{\lambda,\mathrm{wg}} = -\frac{1}{H_{\mathrm{wg}}}\ln\left(\frac{T_{\lambda,\mathrm{wg}}}{1 - R_{\lambda,\mathrm{wg}}}\right) \tag{13}$$

where H_{wg} is the thickness of the waveguide sample.

The properties of the luminophore particles ($\kappa_{\lambda,\mathrm{p}}$, $\sigma_{\mathrm{s}\lambda,\mathrm{p}}$ and $\Phi_{\mathrm{s}\lambda,\mathrm{p}}$) depend not only on the material type, but also on their concentration, shape and alignment. When the luminophore volume fraction is low ($<$ 0.006), the clearance between particles will be large enough that independent scattering can be assumed [11], leading to the following relation for uniform luminophore particle size aligned at a certain tilt angle (assumption (x)):

$$\kappa_{\lambda,\mathrm{p}} = N_{\mathrm{p}}C_{\mathrm{abs,p}} \tag{14}$$

$$\sigma_{\mathrm{s}\lambda,\mathrm{p}} = N_{\mathrm{p}}C_{\mathrm{sca,p}} \tag{15}$$

$$\Phi_{\mathrm{s}\lambda,\mathrm{p}}(\hat{s}',\hat{s}) = \Phi_{\mathrm{sca,p}}(\hat{s}',\hat{s}) \tag{16}$$

where N_{p}, $C_{\mathrm{abs,p}}$, $C_{\mathrm{sca,p}}$, and $\Phi_{\mathrm{sca,p}}$ are the luminophore particle number density, the absorption cross section, the scattering cross section, and the scattering phase function of a single particle, respectively. The determination of the particle-level properties of $C_{\mathrm{abs,p}}$, $C_{\mathrm{sca,p}}$ and $\Phi_{\mathrm{sca,p}}$can refer to one of the two modelling approaches depending on the particle shape: (i) Lorenz–Mie theory for spherical particles [11,27], and

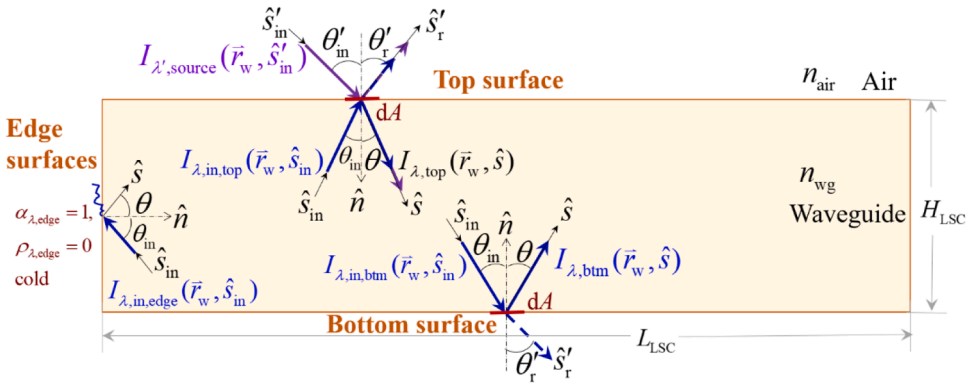

Fig. 2. Schematic of the outgoing ($\hat{n}\cdot\hat{s} > 0$) spectral intensity specified at each boundary surface of the LSC (front view of Fig. 1a, not to scale).

(*ii*) discrete dipole approximation for non-spherical particles of arbitrary shape [28]. Both approaches require the knowledge of the complex refractive index of the luminophore material, which can be predicted by classical theories [27] or measured experimentally [29]. When the luminophore concentration is so high that independent scattering becomes invalid, the properties of $\kappa_{\lambda,\mathrm{p}}$, $\sigma_{\mathrm{s}\lambda,\mathrm{p}}$ and $\Phi_{\mathrm{s}\lambda,\mathrm{p}}$ can be determined either theoretically [30,31] or experimentally [32]. On the other hand, if the complex refractive index of the luminophore material is simply not available, one needs to rely on experimental techniques [32,33] to determine these properties (including the anisotropic absorption coefficient $\kappa_{\lambda,\mathrm{p}}(\hat{s})$), regardless of the luminophore concentration, particle shape and alignment configuration in the LSC.

Finally, the PLQY ϕ_{PL}, and PL wavelength function $P_{\mathrm{PL}\lambda,\mathrm{p}}(\lambda)$of the luminophore can be determined experimentally using a fluorometer–integrating sphere setup [34] and a fluorometer [35], respectively. For luminophores that emit anisotropically, the PL phase function $\Phi_{\mathrm{PL}\lambda,\mathrm{p}}(\hat{s})$ can be determined using a spectrofluorometer equipped with polarizers [19].

2.3. Boundary conditions

The modified RTE, Eq. (7), is a steady-state, first-order differential equation for the spectral intensity in an arbitrary direction $\hat{s}$, so only one boundary condition is required for each direction in order to solve it. The spectral intensity leaving a wall into direction $\hat{s}$ will be specified in the following.

For the top surface, the outgoing intensity towards the waveguide is composed of both the refracted intensity of the incident light from air to waveguide and the reflected intensity within the waveguide itself (see Fig. 2). The refracted intensity $I_{\lambda,\mathrm{refract}}(\vec{r}_{\mathrm{w}},\hat{s}(\theta))$ can be calculated based on radiative energy balance:

$$\left(1-\rho_{\lambda,\mathrm{top,air}}(\theta'_{\mathrm{in}},\theta'_{\mathrm{r}})\right)\cdot I_{\lambda',\mathrm{source}}\left(\vec{r}_{\mathrm{w}},\hat{s}'(\theta'_{\mathrm{in}})\right)\cdot(\mathrm{d}A\cos\theta'_{\mathrm{in}})\mathrm{d}\Omega'\mathrm{d}\lambda'\mathrm{d}t = I_{\lambda,\mathrm{refract}}\left(\vec{r}_{\mathrm{w}},\hat{s}(\theta)\right)(\mathrm{d}A\cos\theta)\mathrm{d}\Omega\mathrm{d}\lambda\mathrm{d}t \tag{17}$$

where $I_{\lambda',\mathrm{source}}$ is the external spectral intensity incident on the top surface of LSC. For collimated irradiation impinged onto the LSC in the direction of $\hat{s}'_{\mathrm{in}}$, we have:

$$I_{\lambda',\mathrm{source}} = q''_{\lambda',\mathrm{source}}\delta(\hat{s}-\hat{s}'_{\mathrm{in}}) \tag{18}$$

where $q''_{\lambda',\mathrm{source}}$ is the radiative flux of the light source, and δ is the Dirac delta function defined as:

$$\delta(x) = \begin{cases} 0, & |x| \geq \varepsilon \\ \lim\limits_{\varepsilon\to 0}\dfrac{1}{2\varepsilon}, & |x| < \varepsilon \end{cases} \tag{19}$$

The solid angle in Eq. (17) can be eliminated using $\mathrm{d}\Omega' = \sin\theta'_{\mathrm{in}}\mathrm{d}\theta'_{\mathrm{in}}\mathrm{d}\varphi$ and $\mathrm{d}\Omega = \sin\theta\mathrm{d}\theta\mathrm{d}\varphi$ (the azimuthal angle φ does not change when light passes from air to waveguide). Introducing the Snell's law (assumption (*vii*)) and its differential version, $n_{\mathrm{air}}\sin\theta'_{\mathrm{in}} = n_{\mathrm{wg}}\sin\theta$, $n_{\mathrm{air}}\cos\theta'_{\mathrm{in}}\mathrm{d}\theta'_{\mathrm{in}} = n_{\mathrm{wg}}\cos\theta\mathrm{d}\theta$, along with the differential version of the wavelength relation $n_{\mathrm{air}}\mathrm{d}\lambda' = n_{\mathrm{wg}}\mathrm{d}\lambda$, Eq. (17) is simplified to:

$$I_{\lambda,\mathrm{refract}}\left(\vec{r}_{\mathrm{w}},\hat{s}(\theta)\right) = \left(1-\rho_{\lambda,\mathrm{top,air}}(\theta'_{\mathrm{in}},\theta'_{\mathrm{r}})\right)\cdot I_{\lambda',\mathrm{source}}\left(\vec{r}_{\mathrm{w}},\hat{s}'(\theta'_{\mathrm{in}})\right)\cdot\left(\frac{n_{\mathrm{wg}}}{n_{\mathrm{air}}}\right)^3 \tag{20}$$

Consequently, the boundary condition at the top surface is:

$$\begin{aligned} I_{\lambda,\mathrm{top}}\left(\vec{r}_{\mathrm{w}},\hat{s}(\theta)\right)\Big|_{\hat{s}\cdot\hat{n}>0} &= I_{\lambda,\mathrm{refract}}\left(\vec{r}_{\mathrm{w}},\hat{s}(\theta)\right) + I_{\lambda,\mathrm{reflect}}\left(\vec{r}_{\mathrm{w}},\hat{s}(\theta)\right) \\ &= \left(1-\rho_{\lambda,\mathrm{top,air}}(\theta'_{\mathrm{in}},\theta'_{\mathrm{r}})\right)\cdot I_{\lambda',\mathrm{source}}\left(\vec{r}_{\mathrm{w}},\hat{s}'(\theta'_{\mathrm{in}})\right)\cdot\left(\frac{n_{\mathrm{wg}}}{n_{\mathrm{air}}}\right)^3 + \rho_{\lambda,\mathrm{top,wg}}(\theta_{\mathrm{in}},\theta)\cdot I_{\lambda,\mathrm{in,top}}\left(\vec{r}_{\mathrm{w}},\hat{s}_{\mathrm{in}}(\theta_{\mathrm{in}})\right) \end{aligned} \tag{21}$$

where $I_{\lambda,\mathrm{in,\ top}}$ is the internal spectral intensity incident on the top surface within the waveguide.

In terms of the bottom surface, the outgoing spectral intensity is composed of self-reflected intensity only (see Fig. 2):

$$I_{\lambda,\mathrm{btm}}\left(\vec{r}_{\mathrm{w}},\hat{s}\right)\Big|_{\hat{s}\cdot\hat{n}>0} = \rho_{\lambda,\mathrm{btm,wg}}(\theta_{\mathrm{in}},\theta)\cdot I_{\lambda,\mathrm{in,btm}}\left(\vec{r}_{\mathrm{w}},\hat{s}_{\mathrm{in}}(\theta_{\mathrm{in}})\right) \tag{22}$$

The bi-directional spectral specular reflectivity terms ($\rho_{\lambda,\mathrm{top,\ air}}$, $\rho_{\lambda,\mathrm{top,\ wg}}$ and$\rho_{\lambda,\mathrm{btm,\ wg}}$) appearing in Eqs. (17), (20)–(22) can be readily determined from Fresnel's relation [11] (assumption (*vii*)):

$$\rho_{\lambda,\mathrm{top,air}} = \frac{1}{2}\left[\left(\frac{\cos\theta - n_{\mathrm{wg}}\cos\theta'_{\mathrm{in}}}{\cos\theta + n_{\mathrm{wg}}\cos\theta'_{\mathrm{in}}}\right)^2 + \left(\frac{\cos\theta'_{\mathrm{in}} - n_{\mathrm{wg}}\cos\theta}{\cos\theta'_{\mathrm{in}} + n_{\mathrm{wg}}\cos\theta}\right)^2\right] \tag{23}$$

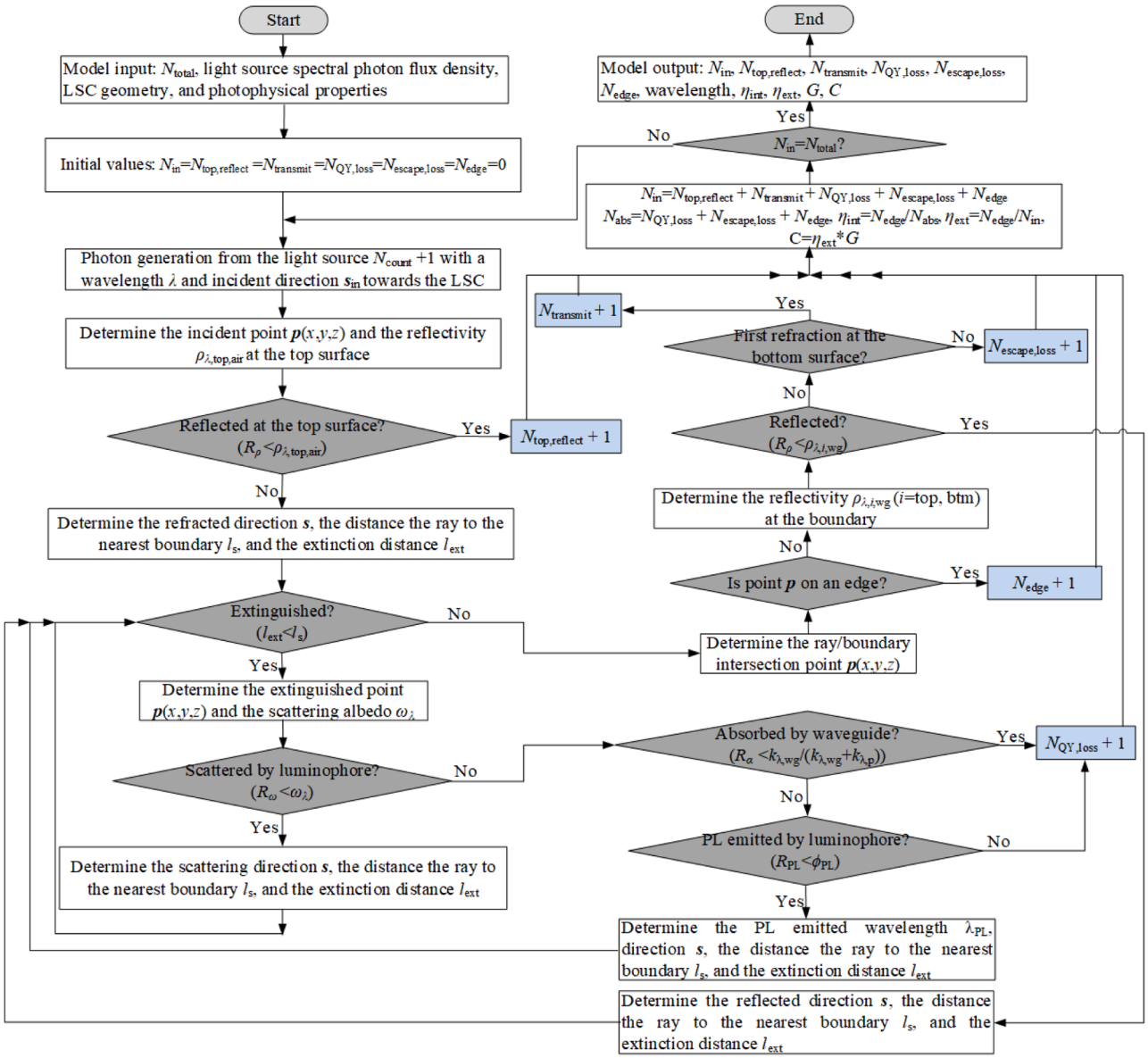

Fig. 3. Flowchart of the MC ray tracing procedure to solve the modified RTE for a 3D planar LSC doped with a generic luminophore.

$$\rho_{\lambda,\mathrm{btm,wg}}=\rho_{\lambda,\mathrm{top,wg}}=\begin{cases}\frac{1}{2}\left[\left(\frac{n_{\mathrm{wg}}\cos\theta_{\mathrm{r}}'-\cos\theta_{\mathrm{in}}}{n_{\mathrm{wg}}\cos\theta_{\mathrm{r}}'+\cos\theta_{\mathrm{in}}}\right)^2+\left(\frac{\cos\theta_{\mathrm{r}}'-n_{\mathrm{wg}}\cos\theta_{\mathrm{in}}}{\cos\theta_{\mathrm{r}}'+n_{\mathrm{wg}}\cos\theta_{\mathrm{in}}}\right)^2\right], & \theta_{\mathrm{in}}<\sin^{-1}\left(1/n_{\mathrm{wg}}\right)\\ 1, & \theta_{\mathrm{in}}\geq\sin^{-1}\left(1/n_{\mathrm{wg}}\right).\end{cases} \tag{24}$$

Finally, for the edge surfaces, the assumptions of perfect absorber (assumption (*viii*)) and cold medium (assumption (*ix*)) lead to the following boundary condition (see Fig. 2):

$$I_{\lambda,\mathrm{edge}}\left(\vec{r}_{\mathrm{w}},\hat{s}\right)\Big|_{\hat{s}\cdot\hat{n}>0}=0 \tag{25}$$

2.4. Solution via Monte Carlo method

Given that the modified RTE (Eq. (7)) for the LSC is a complicated integral–differential equation as a function of location, direction and wavelength, solving it using conventional numerical techniques (finite volume method, spherical harmonics method, zonal method, etc.) would become extremely difficult. On the other hand, such a problem can be readily solved by the MC method in which the history of a large number of photons is traced and spectrally resolved to any degree of accuracy [9, 36].

A flowchart describing the MC ray tracing procedure for a generic 3D planar LSC (Fig. 1) is illustrated in Fig. 3. In the following, photons and rays will be used interchangeably. Since the MC method has been well established to solve the conventional RTE [11,37], here we will mainly

focus on handling the new PL emission term in Eq. (7), and the spectral resolution of photons generated from both the light source and the luminophore. When a photon is emitted from the light source, its spectrum is determined using random sampling of the cumulative distribution function of its spectral photon flux density $\psi_{\lambda,\text{source}}$:

$$\lambda = f^{-1}(R_\lambda),\ \text{with}\ R_\lambda = \frac{\int_{\lambda_{\min}}^{\lambda} \psi_{\lambda,\text{source}} \mathrm{d}\lambda}{\int_{\lambda_{\min}}^{\lambda_{\max}} \psi_{\lambda,\text{source}} \mathrm{d}\lambda} \tag{26}$$

where R_λ is a pseudorandom number uniformly generated between 0 and 1, and f^{-1} represents the inverse function. The same strategy is also used to determine the PL emission spectrum λ_{PL} based on its wavelength function $P_{\text{PL}\lambda,\text{p}}$:

$$\lambda_{\text{PL}} = f^{-1}(R_{\lambda,\text{PL}}),\ \text{with}\ R_{\lambda,\text{PL}} = \frac{\int_{\lambda_{\min}}^{\lambda} P_{\text{PL}\lambda,\text{p}} \mathrm{d}\lambda}{\int_{\lambda_{\min}}^{\lambda_{\max}} P_{\text{PL}\lambda,\text{p}} \mathrm{d}\lambda} \tag{27}$$

Again, $R_{\lambda,\text{PL}}$ is a pseudorandom number. If the incident ray is refracted from the top surface into the waveguide matrix, it can directly reach the boundary or be extinguished (absorbed or scattered) in the midway. The extinction distance l_{ext} is determined as:

$$l_{\text{ext}} = \frac{1}{\beta_\lambda} \ln \frac{1}{R_\beta} \tag{28}$$

where R_β is another pseudorandom number. Handling the photon absorption by the luminophore differs from that by the waveguide which does not re-emit. If the photon is absorbed by the waveguide, it will be directly lost and recorded as QY loss. If otherwise the photon is absorbed by the luminophore, it has the probability to be re-emitted at a different wavelength λ_{PL} (see Eq. (27)). The re-emission direction will be determined based on the PL phase function $\Phi_{\text{PL}\lambda,\text{p}}$, the same strategy as determining the scattering direction [11,37]. The PL emitted photon will go through similar events until its fate is recorded in one of the following: escape cone loss, QY loss, or edge collection. To make the MC method statistically meaningful, a large number of photons (usually on the order of 10^8 or above depending on the size of LSC and the light source spectrum) is required to repeat the ray tracing procedure. The fate of all photons will be recorded in order to determine the performance metrics defined in the upcoming section.

2.5. Performance metrics

The key performance metrics for the LSC as a photonic device are the internal and external photon (or quantum) efficiencies following the protocols proposed in Ref. [38]:

$$\eta_{\text{int}} = \frac{\sum_{i=1}^{4}\sum_{\lambda} \dot{N}_{\lambda,\text{edge},i}}{\sum_{\lambda} \dot{N}_{\lambda,\text{abs}}} = \frac{\sum_{i=1}^{4} \int_{A_{\text{edge}}} \int_{4\pi} \int_{\lambda} I_{\lambda,\text{edge},i}(\lambda, \hat{s}_{\text{in}}) \frac{\lambda}{hc} \mathrm{d}\lambda \cdot \mathrm{d}\Omega_{\text{in}} \cdot |\hat{n}\cdot\hat{s}_{\text{in}}| \mathrm{d}A}{\int_{A_{\text{top}}} \int_{4\pi} \int_{\lambda} I_{\lambda,\text{refract,top}}(\lambda, \hat{s}) \cdot \left(1 - 10^{-(\kappa_{\lambda,\text{wg}} + \kappa_{\lambda,\text{p}} + \sigma_{\text{s}\lambda,\text{p}}) H_{\text{LSC}}}\right) \cdot \frac{\lambda}{hc} \mathrm{d}\lambda \cdot \mathrm{d}\Omega \cdot |\hat{n}\cdot\hat{s}| \mathrm{d}A} \tag{29}$$

$$\eta_{\text{ext}} = \frac{\sum_{i=1}^{4}\sum_{\lambda} \dot{N}_{\lambda,\text{edge},i}}{\sum_{\lambda} \dot{N}_{\lambda,\text{in}}} = \frac{\sum_{i=1}^{4} \int_{A_{\text{edge}}} \int_{4\pi} \int_{\lambda} I_{\lambda,\text{edge},i}(\lambda, \hat{s}_{\text{in}}) \frac{\lambda}{hc} \mathrm{d}\lambda \cdot \mathrm{d}\Omega_{\text{in}} \cdot |\hat{n}\cdot\hat{s}_{\text{in}}| \mathrm{d}A}{\int_{A_{\text{top}}} \int_{4\pi} \int_{\lambda'} I_{\lambda',\text{source}}(\lambda', \hat{s}) \cdot \frac{\lambda'}{hc} \mathrm{d}\lambda' \cdot \mathrm{d}\Omega \cdot |\hat{n}\cdot\hat{s}| \mathrm{d}A} \tag{30}$$

where $\dot{N}_{\lambda,\text{edge},i}$, $\dot{N}_{\lambda,\text{abs}}$, and $\dot{N}_{\lambda,\text{in}}$ are the spectral photon rates collected at edge i, absorbed by the LSC, and incident on the LSC, respectively. The internal photon (or quantum) efficiency is a measure of the quality of light transport process after photon absorption, which is independent of both the light source and absorption spectra. While on the other hand, the external photon (or quantum) efficiency captures the whole light transport process and is more relevant for evaluating the commercial viability of an LSC. Finally, the concentration factor C can be readily determined from $C = G \cdot \eta_{\text{ext}}$, where G is the geometric gain defined as the area ratio of top surface to edge surfaces $G = A_{\text{top}} / \sum_i A_{\text{edge},i}$.

3. Application to LSCs doped with Lumogen F Red 305 with random orientation

The modelling framework described above is applied to investigate the LSCs composed of PMMA as the waveguide matrix doped with a commercial organic dye LFR305, the benchmark luminophore widely

Table 1
Summary of model parameters for MC ray tracing simulation.

Parameter	Baseline value	Parametric values	Unit
L_{LSC}	20	5–150	cm
H_{LSC}	5	2–10	mm
c_{p}	2×10^{-4}	1×10^{-5}–3×10^{-3}	mol/L
$n_{\text{wg,hypo}}$	1.49	1.1–3.3	–
$\phi_{\text{PL,hypo}}$	0.94	0.5–0.99	–
$\Delta\lambda_{\text{S,hypo}}$	33	0–100	nm

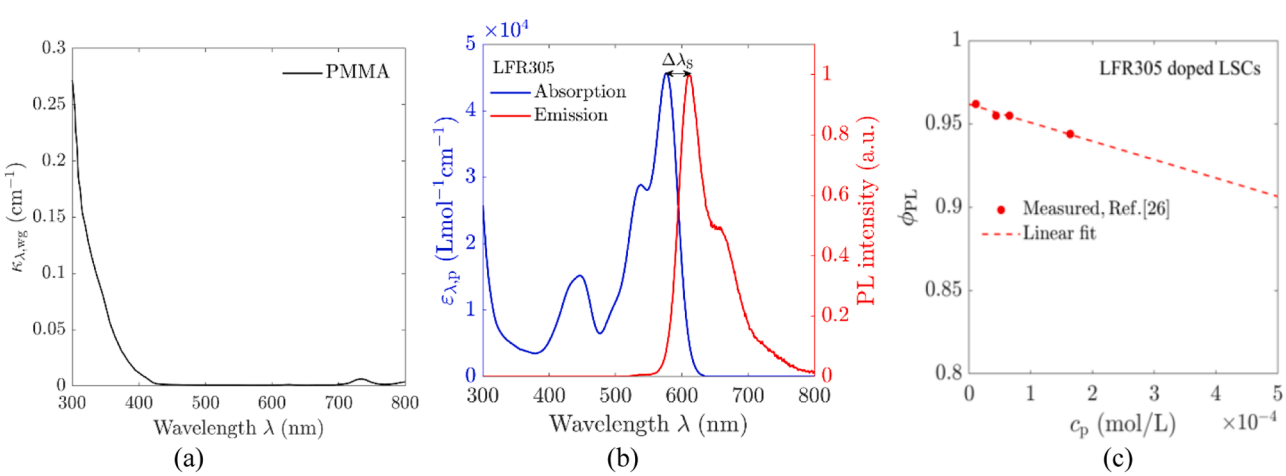

Fig. 4. Photophysical properties of LSCs composed of PMMA doped with varying concentrations of LFR305 dye: (a) spectral absorption coefficient of PMMA from Wilson [47], (b) spectral molar absorption coefficient (left y-axis) and normalized PL emission spectrum (right y-axis) of LFR305 from Zhang et al. [8], and (c) PLQY at varying LFR305 concentrations from Tummeltshammer et al. [34].

employed in the field of LSC [17,39,40]. Note that the LFR305 particles under study are isotropically distributed in the LSC with random orientation instead of aligned at a specific angle. Most of the LFR305 based LSCs are in the form of thin-film type [40,41] and are often investigated together with photovoltaic cells for electricity generation [42], while only limited efforts have been made to study its doped counterpart and to treat it as an independent photonic device. The thin-film type is relatively less efficient given its somewhat low PLQY (in comparison to that of doped LSCs as shown in Fig. 4c) that sharply decreases with the LFR305 concentration (from 0.70 at 1 wt% to 0.55 at 10 wt%) [41]. Though the framework is developed for doped LSCs, the methodology can be readily extended to thin-film LSCs with modified boundary conditions at the film–waveguide interface. In addition, there is a lack of systematic studies on the impact of both the waveguide and luminophore properties in order to analyze different loss mechanisms [17,34,43], which is crucial for designing efficient LSCs.

3.1. Photophysical properties

Unlike other types of luminophore such as inorganic phosphors [9,44] or quantum dots [45] that are essentially scattering, the LFR305 is a non-scattering organic dye, so both the scattering coefficient and scattering phase function in Eq. (7) become zero: $\sigma_{s\lambda,p} = \Phi_{s\lambda,p} = 0$. Since the LFR305 dye molecules are planar π-conjugated systems, their molecular absorption and PL emission are anisotropic [18]. However, the absorption and emission of an ensemble of highly doped isotropically distributed dye particles with random orientation can be treated as isotropic [46]. This treatment can be justified with a thought experiment where collimated light incident on the randomly oriented dye particles from any direction should result in the same absorption and emission behavior. As to LSCs with low dye concentration (~85% peak absorption [46]), the infinitesimal volume (see Fig. 1(b)) used to derive the modified RTE does not contain sufficient dye particles to statistically represent all orientations, and its absorption and PL emission behavior should be treated as anisotropic instead. Nevertheless, given the lack of such anisotropic data for the LFR305 dye in literature, both the absorption and PL emission are assumed isotropic for all doped LSCs investigated here, regardless of their dye concentration. Therefore, we urge caution on the predicted efficiencies for LSCs with low dye concentration (below 85% peak absorption, which corresponds to a dye concentration below 3.66×10^{-5} mol/L), but we believe the efficiency trend should hold. For the study on LSCs using aligned luminophores with anisotropic emission, readers are referred to the work by Moraitis et al. [19]. The photophysical properties of the LFR305 doped in PMMA can be determined following the approach described in Section 2.2, and are found available from literature [8,34,47] as shown in Fig. 4. Note that the absorption coefficient of LFR305 in Fig. 4b is the spectral molar absorption coefficient $\varepsilon_{\lambda,p}$, and its relation to the spectral absorption coefficient $\kappa_{\lambda,p}$ is given by [47]:

$$\varepsilon_p = \frac{\kappa_{\lambda,p}}{c_p}\log_{10}e \tag{31}$$

where c_p is the molar concentration of luminophore particles assuming that Beer–Lambert law is valid within the range of LFR305 concentration (see Table 1). It is obvious that the absorption spectrum of PMMA mainly lies in 300–400 nm, while that of LFR305 extends towards the visible spectrum of up to 620 nm, so competition in light absorption between PMMA and LFR305 occurs in the UV range only. The PL emission spectrum of LFR305 is roughly in the range of 570–800 nm, and an overlap of 570–620 nm exists between its absorption and emission spectrum, leading to PL re-absorption for downstream light transport process. Note there is a red shift in the peak intensity between the absorption and emission spectrum $\Delta\lambda_S$, a phenomenon known as Stokes shift, and its effect will be investigated hypothetically in Section 3.3.2. The PLQY of LSCs doped with LFR305 is found independent of the excitation wavelength [34], and decreases linearly with the dye concentration but always stays above 93% when LFR305 concentration is below 2×10^{-4} mol/L. A linear fit of PLQY with c_p as shown in Fig. 4c will be employed to facilitate the investigation on the effect of dye concentration later in Section 3.3.1.

3.2. Numerical solution and validation

Once the photophysical properties are available, Eq. (7) along with its boundary conditions (Eqs. (21)–(25)) can be readily solved using the MC ray tracing approach (see Fig. 3). Here, we only consider the scenario where the light source is normally incident on the LSC ($\theta'_{in} = 0°$) in order to explore the LSC performance under varying design and material choices. Readers are referred to Ref. [48] for the effect of light incident angle. A number of open-source MC codes are available in literature [8,9,49,50], and the one developed by Zhang et al. [8] is adopted here with modifications including: (*i*) instead of the AM 1.5D solar spectral irradiance (Fig. S1a), its spectral photon flux density (see Fig. S1b) is used as the light source in order to be consistent with the quantum nature of the performance metrics as defined in Section 2.5, and (*ii*) light losses via top reflection and bottom transmission are further distinguished to quantify different loss mechanisms. For each simulation, the AM1.5D solar irradiance spectrum is equally discretized into 3701 wavelengths between 300 and 4000 nm with a spectral resolution of 1 nm. If a light source with narrower spectral range (300–1000 nm for example) is implemented, a higher external photon efficiency will be predicted than that using the AM1.5D solar spectrum. A ray number independence check is needed to warrant sufficient confidence in the result, and an example case is put in Table S1. To validate the MC ray tracing model, the experimental data of LSCs doped with Coumarin 6 at varying dye concentrations reported by Tummeltshammer et al. [34] are used, and the root-mean-square error between measurement and simulation is 1.4% as shown in Fig. S2.

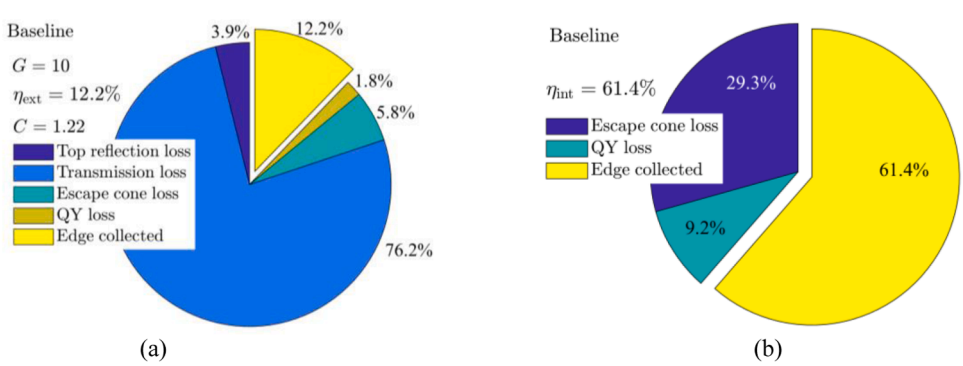

Fig. 5. LSC baseline performance in terms of (a) external photon fate, and (b) internal photon fate.

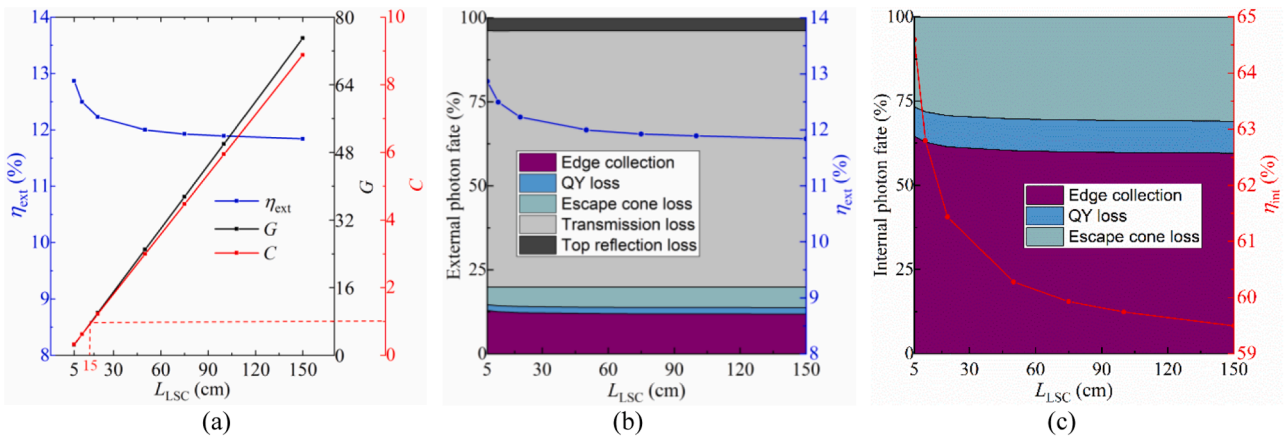

Fig. 6. Effect of LSC length on: (a) external photon efficiency (left *y*-axis), geometric gain and concentration factor (right *y*-axes), (b) external photon fate (left *y*-axis) and external photon efficiency (right *y*-axis), and (c) internal photon fate (left *y*-axis) and internal photon efficiency (right *y*-axis) of LFR305 doped LSCs. Other parameters are kept constant at their baseline values as listed in Table 1.

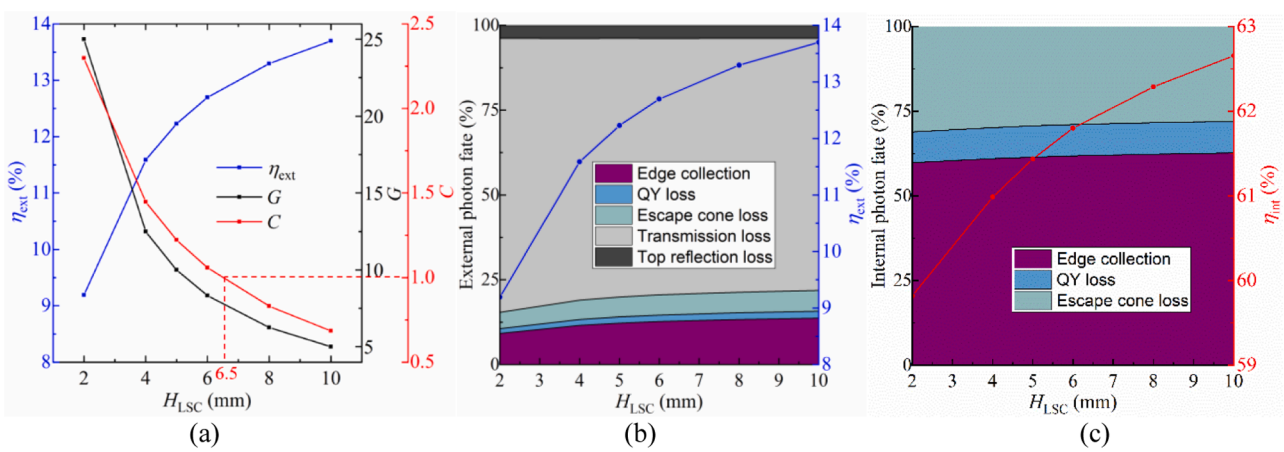

Fig. 7. Effect of LSC thickness on: (a) external photon efficiency (left *y*-axis), geometric gain and concentration factor (right *y*-axes), (b) external photon fate (left *y*-axis) and external photon efficiency (right *y*-axis), and (c) internal photon fate (left *y*-axis) and internal photon efficiency (right *y*-axis) of LFR305 doped LSCs. Other parameters are kept at their baseline values as listed in Table 1.

3.3. Performance analysis

The key model parameters used for the MC ray tracing simulation are summarized in Table 1 which includes both the baseline and parametric scenarios. The baseline case is a square shaped LSC (L_{LSC}=W_{LSC}) with dimensions of 20 cm × 20 cm × 5 mm composed of PMMA as the waveguide with a spectral average refractive index of 1.49 doped with LFR305 dye at a concentration of 2 × 10^{-4} mol L^{-1} with 94% PLQY

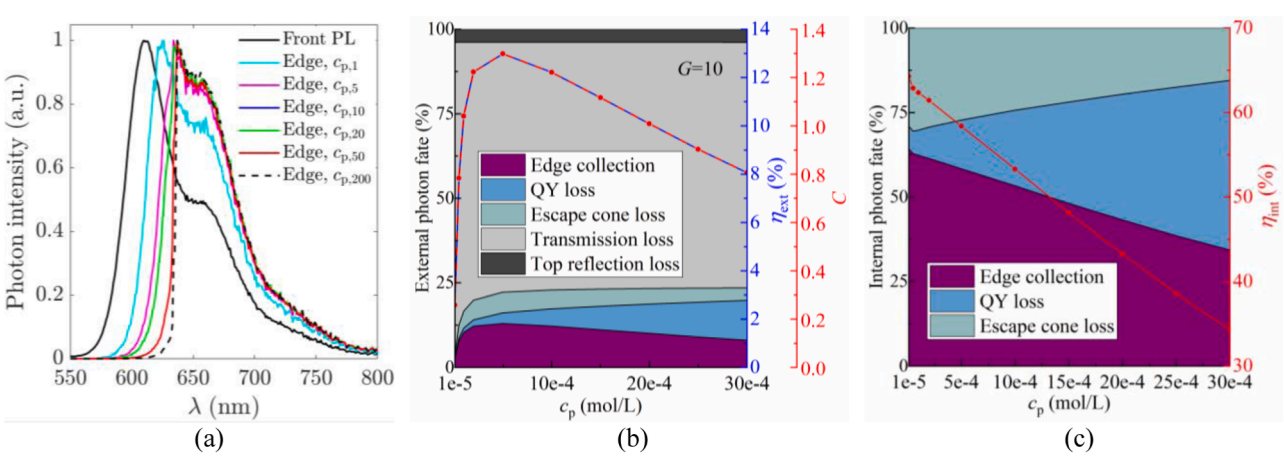

Fig. 8. Effect of dye concentration on: (a) normalized photon intensity collected at edges versus front-face PL emission, (b) external photon fate (left *y*-axis), external photon efficiency and concentration factor (right *y*-axes), and (c) internal photon fate (left *y*-axis) and internal photon efficiency (right *y*-axis) of LFR305 doped LSCs. Note that $c_{p,\#}$ in the legend of subfigure (a) represents # × 10^{-5} mol/L, and other parameters are kept at their baseline values as listed in Table 1.

(Fig. 4c). The parametric case is aimed to examine the effects of certain geometric and material parameters, under both realistic and hypothetical scenarios. The realistic scenarios consider the effects of LSC length and thickness, as well as the molar concentration of LFR305, while the hypothetical scenarios assume different material properties, such as the waveguide refractive index, the PLQY of the luminophore particles, and the Stokes shift. Note that the parametric study will be conducted by varying the variable of interest within its range while keeping all other parameters constant at their baseline values, unless stated otherwise.

3.3.1. Realistic scenarios

3.3.1.1. Baseline scenario. Fig. 5 displays the baseline performance for both external and internal photon fates. Among all external loss mechanisms, transmission loss is the dominating pathway (76.2%), followed by the escape cone loss (5.8%) and the top reflection loss (3.9%). This is mainly due to the low fraction of the LFR305 absorption spectrum (300–620 nm) within the broadband solar spectrum (300–4000 nm) and also to the non-scattering nature of LFR305, leaving most sunlight, particularly those outside the LFR305 absorption spectrum, directly lost via bottom transmission. The QY loss is the lowest (1.8%) mainly due to the high value of PLQY (0.94). Consequently, an external photon efficiency of 12.2% and a concentration factor of 1.22 are predicted for the baseline LSC. The escape cone loss dominates over the QY loss (29.3% vs 9.2%) among the internal photon fates after light absorption, a result of the PMMA refractive index of 1.49 and high PLQY of 0.94. The internal photon efficiency is 61.4%.

3.3.1.2. Effect of geometric parameters. The effect of LSC length is shown in Fig. 6 for both the external and internal light transport processes while holding other parameters unchanged at their baseline values. As the LSC length significantly increases, a minor decrease of 8.0% is observed in the external photon efficiency, from 12.9% at 5 cm length to 11.8% at 150 cm. This indicates that the performance of a lab-scale LSC can be roughly maintained for a pilot-scale device, implying good scale-up potential that is crucial for future commercial deployment. As a result, a monotonic increase is observed for the concentration factor—from 0.32 at 5 cm length to 8.9 at 150 cm—owing to the dominating effect of linear increase in the geometric gain (Fig. 6a).

Given the constant contribution from the top reflection loss (3.9%) and the transmission loss (76.2%) as shown in Fig. 6b, the LSC length is found to mainly affect the internal light transport process. A larger LSC represents longer light transport path that will trigger more PL re-absorption events by downstream LFR305 particles, leading to both higher escape cone loss and QY loss (Fig. 6c). Consequently, the internal photon efficiency decreases monotonically with higher L_{LSC}, from 64.6% at 5 cm length to 59.5% at 150 cm. In light of these results, a larger LSC at meter scale is recommended to aim for high concentration factor while still maintaining a good external photon efficiency of above 11%.

Fig. 7 illustrates the effect of LSC thickness on its performance. As the LSC thickness increases from 2 mm to 10 mm, the geometric gain drops by 80% (from 25 to 5), which is also accompanied by a 49% increase in the external photon efficiency (from 9.2% to 13.7%). These two counteracting effects eventually lead to lower concentration factor (from 2.3 at 2 mm thickness to 0.7 at 10 mm) because the decrease in the geometric gain is more dominating (Fig. 7a). For the external light transport process (Fig. 7b), a higher LSC thickness signifies a longer path along the light incidence direction, leading to enhanced light absorption and hence a decreased transmission loss from 80.8% at 2 mm thickness to 74.3% at 10 mm. Consequently, more photons will be PL emitted and guided to the edges via TIR, though the escape cone and QY losses also increase slightly. As to the internal photon transport process (Fig. 7c), a sublinear increase trend is found for η_{int} as the LSC becomes thicker, mainly due to the drop in escape cone loss—from 31.1% at 2 mm thickness to 28.0% at 10 mm—among the absorbed photons. The highest η_{int} of 62.7% is achieved at a thickness of 10 mm. Given the opposite trends observed in C and η_{ext}, a tradeoff needs to be made between high concentration factor and high external photon efficiency when designing the LSC thickness. However, care must be taken to ensure a thickness of less than 6.5 mm in order to avoid achieving an undesirable concentration factor below one.

3.3.1.3. Effect of dye concentration. Fig. 8a displays the normalized photon intensity collected at the edges at varying LFR305 concentration versus front-face PL emission (see Fig. 4b). It is obvious that the edge photon spectrum resembles the front-face PL emission, confirming light transport via TIR by the waveguide of the PL emission from LFR305 towards the edges. As the dye concentration increases, the edge photon peak spectrum becomes red-shifted in comparison to the front-face PL spectrum due to the downstream re-absorption effect, from 12 nm at 1×10^{-5} mol/L to 27 nm at 5×10^{-4} mol/L, beyond which the red-shift in peak spectrum remains unchanged. The external photon efficiency and the concentration factor (right y-axes) along with the fractional photon fate (left y-axis) are shown in Fig. 8b to reveal different loss mechanisms. Dye concentration mainly affects the transmission loss and the QY loss. As the dye concentration increases, the sunlight absorption continues to rise until reaching its plateau, leading to a first-decrease-then-saturated trend in the transmission loss given the constant reflection loss at the top surface (3.9%). On the other hand, higher LFR305 concentration also signifies lower PLQY (Fig. 4c) thus higher QY loss due to the enhanced

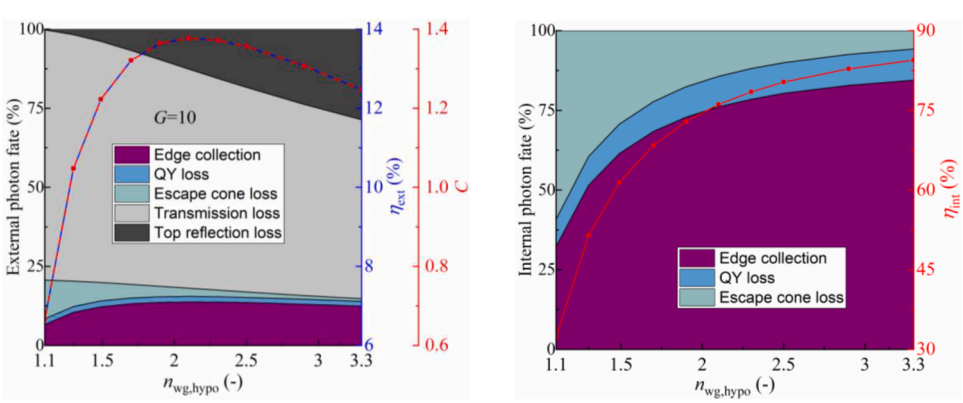

Fig. 9. Effect of hypothetical refractive index of the waveguide on: (a) external photon fate (left y-axis), external photon efficiency and concentration factor (right y-axes), and (b) internal photon fate (left y-axis) and internal photon efficiency (right y-axis) of LSCs composed of a hypothetical waveguide material doped with LFR305 dye at a concentration of 1×10^{-4} mol/L. Note that all other photophysical properties and model parameters remain the same as shown in Fig. 4 and Table 1 (baseline values), respectively.

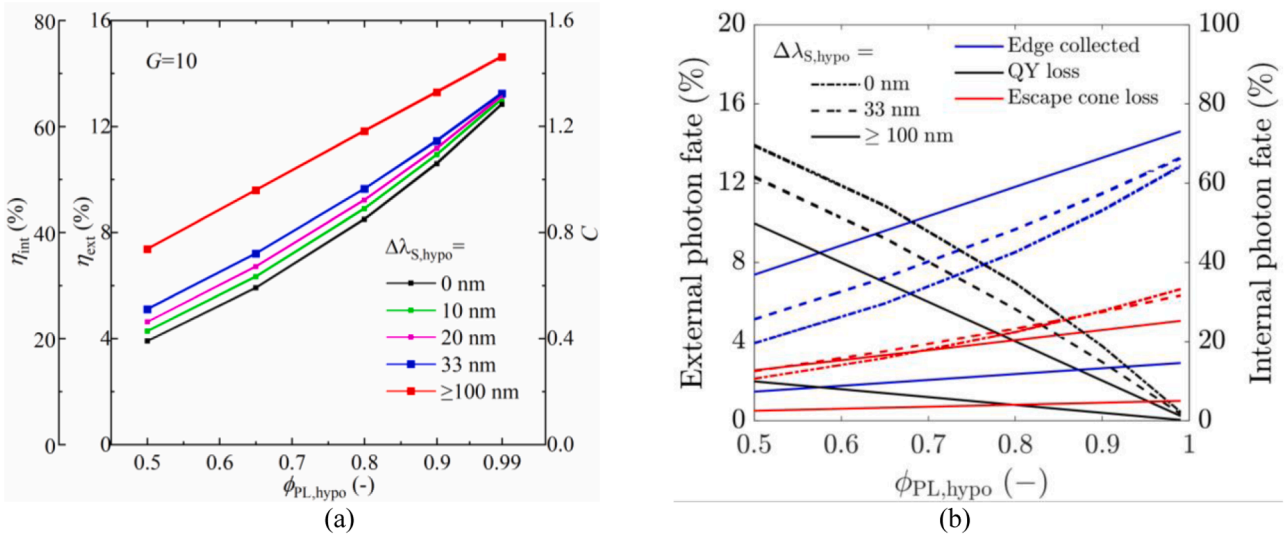

Fig. 10. Effect of hypothetical PLQY on: (a) external and internal photon efficiencies (left *y*-axes) and concentration factor (right *y*-axis), and (b) external (left *y*-axis) and internal photon fates (right *y*-axis) of LSCs composed of PMMA as the waveguide material doped with hypothetical luminophores at varying Stokes shift scenarios. Note that all other photophysical properties and model parameters remain the same as shown in Fig. 4 and Table 1 (baseline values), respectively.

PL quenching effect. Consequently, a non-trivial trend is observed for both the external photon efficiency and the concentration factor, and the best performance is achieved at an optimal concentration of around 5×10^{-4} mol/L with a peak η_{ext} of 13.0% and a peak C of 1.3. The concentration factor follows the same trend as the external photon efficiency given the constant geometric gain maintained at 10. For the internal transport process after light absorption (Fig. 8c), η_{int} is found to decrease monotonically as LFR305 concentration increases—from 64.3% at 1×10^{-5} mol/L to 34.3% at 3×10^{-3} mol/L, mainly due to the enhanced QY loss that dominates over the decreased escape cone loss at higher c_p. Similar trends in both η_{ext} and η_{int} have been reported for thin-film LSCs based on LFR305 but with lower performance (maximum η_{ext}=4.9% and η_{int}=28.7%) [41]. Given the different trends observed in the external and internal photon efficiencies, a dye concentration close to its optimum (5×10^{-4} mol/L in our case) aiming for high η_{ext} (also high C) should be recommended, since η_{ext} is a relevant figure of merit for assessing the commercial potential of an LSC.

3.3.2. Hypothetical scenarios

3.3.2.1. Effect of waveguide refractive index. Fig. 9 illustrates the effect of hypothetical refractive index of the waveguide on LSC performances. As $n_{wg,hypo}$ becomes higher, the top reflection loss increases monotonically (see Eq. (23)), but in the meantime, the escape cone loss descends significantly due to the reduction in the critical angle of TIR ($\sin^{-1}(1/n_{wg,hypo})$), leading to a non-trivial trend in the external photon efficiency as observed in Fig. 9a. The best performance is achieved with a peak η_{ext} of 13.8% along with a peak C of 1.38 at an optimal $n_{wg,hypo}$ of around 2.1, which well balances the competing effect between high escape cone loss at low $n_{wg,hypo}$ and high top reflection loss at high $n_{wg,hypo}$. By contrast, the internal photon efficiency is found to increase sub-linearly with higher refractive index, from 32.3% when setting $n_{wg,hypo}$ at 1.1 to 84.4% at 3.3, mainly due to the substantial drop in the escape cone loss that dominates over the slight increase in the QY loss (Fig. 9b). In light of these results, a transparent waveguide material with a refractive index close to 2.1 would be highly desirable to aim for both high external photon efficiency and high concentration factor. However, materials with a refractive index of above 2, like boron nitride and cubic zirconia, usually appear opaque, and are hence not suitable for the LSC application. As a compromise, high-index plastics and glass such as MR-174 (n_{wg} = 1.74 from Mitsui Chemicals, Japan) and 1.9 Glass (n_{wg} = 1.893 from Zhong Chuan Optical, China) could serve as promising waveguide candidates for further investigation.

3.3.2.2. Effects of PLQY and stokes shift. The effect of PLQY of a hypothetical luminophore under varying Stokes shift scenarios is shown in Fig. 10 that illustrates similar trend for all performance metrics (η_{ext}, η_{int} and C). Since the top reflection loss (3.9%) and the transmission loss (76.2%) remain unchanged as PLQY varies, these two terms are not illustrated in the external photon fate (left *y*-axis of Fig. 10b). A stack version of all photon fates is put in Fig. S3. As the PLQY increases, the QY loss drops significantly, leading to remarkable improvement in both the internal and external photon efficiencies as well as the concentration factor, despite the slight increase in escape cone loss. Both the efficiencies and the concentrator factor are increased by 1.6 times—from 25.7% to 66.5% for η_{int}, from 5.1% to 13.2% for η_{ext}, and from 0.5 to 1.3 for C—as PLQY grows from 0.5 to 0.99 at a Stokes shift of 33 nm. As to the effect of Stokes shift, a higher $\Delta\lambda_{S,hypo}$ signifies less overlap between the absorption and emission spectrum thus weaker PL re-absorption, resulting in both lower QY and escape cone losses. Consequently, both efficiencies tend to increase until reaching the threshold Stokes shift at around 100 nm, above which the efficiencies begin to plateau due to the absence of re-absorption effect with zero spectral overlap. In addition, the efficiency improvement is more pronounced at lower PLQY. For instance, the increasement in both efficiencies is 89% (from 19.6% to 37.1% for η_{int} and from 3.9% to 7.4% for η_{ext}) at a PLQY of 0.5 when $\Delta\lambda_{S,hypo}$ rises from 0 nm to 100 nm, while that becomes only 14% (from 64.4% to 73.4% for η_{int} and from 12.8% to 14.6% for η_{ext}) at a PLQY of 0.99. Therefore, a luminophore with both high PLQY and high Stokes shift will be highly desirable for an efficient LSC.

4. Conclusions

A self-consistent modelling framework of radiative transfer has been described for a generic LSC to account for the light–matter interactions at multiple length scales. A modified RTE along with its boundary conditions was rigorously derived based on radiative energy balance, and can be solved using the MC ray tracing approach. Such a framework was then applied to a specific type of square shaped LSC composed of PMMA as the waveguide doped with LFR305 dye as the luminophore, and its performance and losses have been quantified for various scenarios.

The realistic scenarios examined both the baseline performance as well as the effects of LSC dimensions and LFR305 concentration. For the baseline scenario, an external photon efficiency of 12.2% was predicted for the LSC with dimensions of 20 × 20 × 0.5 cm^3 at a LFR305 concentration of 0.0002 mol/L. The transmission loss accounts for 76.2% of the incident photons, and is the dominating loss mechanism fundamentally due to the relatively narrow absorption spectrum of LFR305 within the solar spectrum and the non-scattering nature of LFR305. The LSC length has a minor effect on the external photon efficiency, and an efficiency drop of only 1.1% (from 12.9% to 11.8%) is observed as LSC length increases from 5 cm to 150 cm, demonstrating good scale-up potential. By contrast, the LSC thickness and LFR305 concentration have a more pronounced effect on the LSC performance. A thicker LSC leads to higher external photon efficiency but lower concentration factor, and a thickness of less than 6.5 mm needs to be guaranteed in order to avoid an undesirable concentration factor below 1. The effect of dye concentration mainly affects the transmission loss and the QY loss, and there exists an optimal concentration at around 0.0005 mol/L leading to a peak external photon efficiency of 13.0% along with a peak concentration factor of 1.3. However, the transmission loss still dominates and accounts for 72.6–92.1% depending on the specific thickness and dye concentration.

The hypothetical scenarios aimed to investigate alternative material properties for potential efficiency improvement in order to guide follow-up LSC design. As to the impact of waveguide refractive index (n_{wg}), a non-trivial trend is observed for the external photon efficiency, revealing inevitable tradeoff of competing effects between high escape cone loss at low n_{wg} and high top reflection loss at high n_{wg}. Consequently, an optimal n_{wg} at around 2.1 exists leading to a peak η_{ext} of 13.8% and a peak C of 1.38, an increase of 13.1% as compared to the baseline performance. The hypothetical PLQY and Stokes shift are found to mainly affect the QY loss, and high PLQY combined with high Stokes shift synergistically contributes to improvement in both internal and external photon efficiencies. The best η_{ext} is 14.6% with a concentration factor of 1.46 when PLQY is 0.99 and the Stokes shift is above 100 nm to disable the re-absorption effect. In light of these results, future improvement on LSC efficiency should be focused on mitigating the predominant transmission loss by capturing more sunlight over broadband spectrum, such as using back reflectors (diffuse or specular), multiple luminophores, or tandem LSC configurations.

CRediT authorship contribution statement

Sha Li: Writing – original draft, Software, Methodology, Investigation, Formal analysis, Conceptualization. **Sophia Haussener:** Writing – review & editing, Supervision, Funding acquisition, Conceptualization.

Declaration of competing interest

The authors declare that they have no known competing financial interests or personal relationships that could have appeared to influence the work reported in this paper.

Data availability

Data will be made available on request.

Acknowledgements

The financial support from the EU's Horizon 2020 SPOTLIGHT Project (Grant Agreement No. 101015960) funded by the Photonics Public Private Partnership Programme is gratefully acknowledged.

Supplementary materials

Supplementary material associated with this article can be found, in the online version, at doi:10.1016/j.jqsrt.2024.108957.

References

[1] Papakonstantinou I, Portnoi M, Debije MG. The hidden potential of luminescent solar concentrators. Adv Energy Mater 2020;11(3):2002883.
[2] Gungor K, Du J, Klimov VI. General trends in the performance of quantum dot luminescent solar concentrators (LSCs) revealed using the "effective LSC quality factor. ACS Energy Lett. 2022;7(5):1741–9.
[3] Chatten A, Barnham K, Buxton B, Ekins-Daukes N, Malik M. Quantum dot solar concentrators. Semiconductors 2004;38:909–17.
[4] Chatten A, Farrel D, Jermyn C, Thomas P, Buxton B, Buchtemann A. Thermodynamic modelling of luminescent solar concentrators. In: Conference Record of the Thirty-first IEEE Photovoltaic Specialists Conference, 2005. IEEE; 2005. p. 82–5.
[5] Yablonovitch E. Thermodynamics of the fluorescent planar concentrator. JOSA 1980;70(11):1362–3.
[6] Farrell DJ, Chatten AJ, Buchtemann A, Barnham KW. Fabrication, characterisation & modelling of quantum dot solar concentrator stacks. In: 2006 IEEE 4th World Conference on Photovoltaic Energy Conference. IEEE; 2006. p. 217–20.
[7] Carrascosa M, Unamuno S, Agulló-López F. Monte Carlo simulation of the performance of PMMA luminescent solar collectors. Appl Opt 1983;22(20): 3236–41.
[8] Zhang B, Yang H, Warner T, Mulvaney P, Rosengarten G, Wong WWH. A luminescent solar concentrator ray tracing simulator with a graphical user interface: features and applications. Methods Appl Fluoresc 2020;8(3):037001.
[9] Smith DE, Hughes MD, Patel B, Borca-Tasciuc DA. An Open-Source Monte Carlo Ray-Tracing Simulation Tool for Luminescent Solar Concentrators with Validation Studies Employing Scattering Phosphor Films. Energies 2021;14(2):455.
[10] Kennedy M, Chatten A, Farrell D, Bose R, Büchtemann A, McCormack S. Thermodynamic modelling and ray-trace modelling of luminescent solar concentrators: a comparison of the two approaches. In: 23rd European Photovoltaic Solar Energy Conference and Exhibition; 2008. p. 334–7.
[11] Modest MF. Radiative Heat Transfer. Academic Press; 2013. p. 279–300. Third Edition ed.
[12] Haussener S, Lipiński W, Petrasch J, Wyss P, Steinfeld A. Tomographic characterization of a semitransparent-particle packed bed and determination of its thermal radiative properties. J Heat Transfer 2009;131(7).
[13] Dai X, Haussener S. Optical characterization of multi-scale morphologically complex heterogeneous media–Application to snow with soot impurities. J Q Spectros Radiative Trans 2018;206:378–91.
[14] Verbunt PP, Sanchez-Somolinos C, Broer DJ, Debije MG. Anisotropic light emissions in luminescent solar concentrators-isotropic systems. Opt Express 2013; 21(Suppl 3):A485–93.
[15] Verbunt PPC, Kaiser A, Hermans K, Bastiaansen CWM, Broer DJ, Debije MG. Controlling light emission in luminescent solar concentrators through use of dye molecules aligned in a planar manner by liquid crystals. Adv Funct Mater 2009;19 (17):2714–9.
[16] Alinejad F, Bordbar H, Makowska M, Hostikka S. Spectroscopic determination of the optical constants and radiative properties of black PMMA for pyrolysis modeling. Int J Thermal Sci 2022;176:107501.
[17] Kaniyoor A, McKenna B, Comby S, Evans RC. Design and response of high-efficiency, planar, doped luminescent solar concentrators using organic-inorganic Di-Ureasil waveguides. Adv Opt Mater 2016;4(3):444–56.
[18] Debije MG, Verbunt PPC. Thirty years of luminescent solar concentrator research: solar energy for the built environment. Adv Energy Mater 2012;2(1):12–35.
[19] Moraitis P, de Boer DKG, Prins PT, de Mello Donegá C, Neyts K, van Sark WGJHM. Should anisotropic emission or reabsorption of nanoparticle luminophores be optimized for increasing luminescent solar concentrator efficiency? Sol RRL 2020;4 (10).
[20] Ferreira LV, Costa SM, Pereira EJ. Fluorescence quantum yield evaluation of strongly absorbing dye solutions as a function of the excitation wavelength. J Photochem Photobiol A: Chem 1991;55(3):361–76.
[21] Weber G, Teale F. Fluorescence excitation spectrum of organic compounds in solution. part 1—systems with quantum yield independent of the exciting wavelength. Trans Faraday Soc 1958;54:640–8.
[22] Dramićanin M. Luminescence Thermometry: Methods, Materials, and Applications. Woodhead Publishing; 2018. p. 33–61.
[23] Verbunt PPC, de Jong TM, de Boer DKG, Broer DJ, Debije MG. Anisotropic light emission from aligned luminophores. Eur Phys J Appl Phys 2014;67(1):10201.
[24] Du K, Li H, Guo K, Wang H, Li D, Zhang W. The rate equation based optical model for phosphor-converted white light-emitting diodes. J Phys D Appl Phys 2017;50 (9):095101.
[25] Ma Y, Sun J, Luo X. Multi-wavelength phosphor model based on fluorescent radiative transfer equation considering re-absorption effect. J Lumin 2019;209: 109–15.
[26] Yalcin RA, Erturk H. Monte Carlo method solution of the broadband fluorescent radiative transfer equation considering fluorescent cascade. Appl Opt 2021;60(4): 1068–77.
[27] Bohren CF, Huffman DR. Absorption and Scattering of Light by Small Particles. John Wiley & Sons; 2008. p. 12–56.

[28] Draine BT, Flatau PJ. Discrete-dipole approximation for scattering calculations. Josa A 1994;11(4):1491–9.
[29] Chen J, Wheeler VM, Liu B, Kumar A, Coventry J, Lipiński W. Optical characterisation of alumina–mullite materials for solar particle receiver applications. Solar Energy Mater Solar Cells 2021;230:111170.
[30] Oster G. The scattering of light and its applications to chemistry. Chem Rev 1948; 43(2):319–65.
[31] Oster G, Riley DP. Scattering from isotropic colloidal and macro-molecular systems. Acta Crystallogr 1952;5(1):1–6.
[32] Hughes MD, Borca-Tasciuc DA, Kaminski DA. Method for modeling radiative transport in luminescent particulate media. Appl Opt 2016;55(12):3251–60.
[33] Kamal JS, Gomes R, Hens Z, Karvar M, Neyts K, Compernolle S. Direct determination of absorption anisotropy in colloidal quantum rods. Phys Rev B 2012;85(3).
[34] Tummeltshammer C, Taylor A, Kenyon AJ, Papakonstantinou I. Losses in luminescent solar concentrators unveiled. Solar Energy Mater Solar Cells 2016; 144:40–7.
[35] Zhang B, Soleimaninejad H, Jones DJ, White JM, Ghiggino KP, Smith TA. Highly fluorescent molecularly insulated perylene diimides: effect of concentration on photophysical properties. Chem Mater 2017;29(19):8395–403.
[36] Hughes MD, Maher C, Borca-Tasciuc DA, Polanco D, Kaminski D. Performance comparison of wedge-shaped and planar luminescent solar concentrators. Renew Energy 2013;52:266–72.
[37] Howell JR. Application of Monte Carlo to Heat Transfer Problems. Advances in Heat Transfer. Elsevier; 1969. p. 1–54. 5.
[38] Debije MG, Evans RC, Griffini G. Laboratory protocols for measuring and reporting the performance of luminescent solar concentrators. Energy Environ Sci 2021;14 (1):293–301.
[39] Cambié D, Zhao F, Hessel V, Debije MG, Noel T. A leaf-inspired luminescent solar concentrator for energy-efficient continuous-flow photochemistry. Angew Chem Int Ed Engl 2017;56(4):1050–4.
[40] Griffini G, Levi M, Turri S. Thin-film luminescent solar concentrators: a device study towards rational design. Renew Energy 2015;78:288–94.
[41] Tatsi E, Fortunato G, Rigatelli B, Lyu G, Turri S, Evans RC. Thermoresponsive host polymer matrix for self-healing luminescent solar concentrators. ACS Appl Energy Mater 2019;3(1):1152–60.
[42] Ostos FJ, Iasilli G, Carlotti M, Pucci A. High-performance luminescent solar concentrators based on poly(cyclohexylmethacrylate) (PCHMA) films. Polymers (Basel) 2020;12(12).
[43] Zettl M, Mayer O, Klampaftis E, Richards BS. Investigation of host polymers for luminescent solar concentrators. Energy Technol 2017;5(7):1037–44.
[44] Ma Y, Wang M, Sun J, Hu R, Luo X. Phosphor modeling based on fluorescent radiative transfer equation. Opt Express 2018;26(13):16442–55.
[45] Klimov VI, Baker TA, Lim J, Velizhanin KA, McDaniel H. Quality factor of luminescent solar concentrators and practical concentration limits attainable with semiconductor quantum dots. ACS Photonics 2016;3(6):1138–48.
[46] Debije MG, Verbunt PP, Rowan BC, Richards BS, Hoeks TL. Measured surface loss from luminescent solar concentrator waveguides. Appl Opt 2008;47(36):6763–8.
[47] Wilson LR. Luminescent Solar Concentrators: a Study of Optical Properties, re-Absorption and Device Optimisation. Heriot-Watt University Edinburgh; 2010. PhD thesis.
[48] Hughes MD, Borca-Tasciuc DA, Kaminski DA. Highly efficient luminescent solar concentrators employing commercially available luminescent phosphors. Solar Energy Mater Solar Cells 2017;171:293–301.
[49] Cambié D, Zhao F, Hessel V, Debije MG, Noël T. Every photon counts: understanding and optimizing photon paths in luminescent solar concentrator-based photomicroreactors (LSC-PMs). Reaction Chem Eng 2017;2(4):561–6.
[50] Farrell D., Farrell D. Pvtrace: optical ray tracing for luminescent materials and spectral converter photovoltaic devices. 2019.